HHS Public Access

Author manuscript

Phys Med Biol. Author manuscript; available in PMC 2022 December 29.

Published in final edited form as:

Phys Med Biol. ; 66(24): . doi:10.1088/1361-6560/ac43fd.

Pre- and post-treatment image-based dosimetry in ^{90}Y-microsphere radioembolization using the TOPAS Monte Carlo toolkit

Alejandro Bertolet, PhD,
Department of Radiation Oncology, Massachusetts General Hospital and Harvard Medical School, Boston, MA, USA.

Eric Wehrenberg-Klee, MD,
Department of Radiology, Division of Interventional Radiology, Massachusetts General Hospital, Boston, MA, USA.

Mislav Bobić, MSc,
Department of Radiation Oncology, Massachusetts General Hospital and Harvard Medical School, Boston, MA, USA & Department of Physics, ETH Zürich, Zürich, Switzerland.

Clemens Grassberger, PhD,
Department of Radiation Oncology, Massachusetts General Hospital and Harvard Medical School, Boston, MA.

Joseph Perl, PhD,
SLAC National Accelerator Laboratory, Menlo Park, CA, USA.

Harald Paganetti, PhD,
Department of Radiation Oncology, Massachusetts General Hospital and Harvard Medical School, Boston, MA, USA.

Jan Schuemann, PhD
Department of Radiation Oncology, Massachusetts General Hospital and Harvard Medical School, Boston, MA, USA.

Abstract

Objective: To evaluate the pre-treatment and post-treatment imaging-based dosimetry of patients treated with 90Y-microspheres, including accurate estimations of dose to tumor, healthy liver and lung. To do so, the Monte Carlo (MC) TOPAS platform is in this work extended towards its utilization in radionuclide therapy.

Correspondence: abertoletreina@mgh.harvard.edu.

Conflicts of interest: Eric Wehrenberg-Klee receives preclinical research funding, clinical research funding, and consulting fees from Boston Scientific, and consulting fees and honoraria from Sirtex. The other authors have no conflict of interests to declare.

Ethics approval: Formal consent was not required for this study.

Approach: Five patients treated at the Massachusetts General Hospital were selected for this study. All patients had data for both pre-treatment SPECT-CT imaging using 99mTc-MAA as a surrogate of the 90Y-microspheres treatment and SPECT-CT imaging immediately after the 90Y activity administration. Pre- and post-treatment doses were computed with TOPAS using the SPECT images to localize the source positions and the CT images to account for tissue inhomoegeneities. We compared our results with analytical calculations following the voxel-based MIRD scheme.

Main results: TOPAS results largely agreed with the MIRD-based calculations in soft tissue regions: the average difference in mean dose to the liver was 0.14 Gy/GBq (2.6%). However, dose distributions in the lung differed considerably: absolute differences in mean doses to the lung ranged from 1.2 Gy/GBq to 6.3 Gy/GBq and relative differences from 153% to 231%. We also found large differences in the intra-hepatic dose distributions between pre- and post-treatment imaging, but only limited differences in the pulmonary dose.

Significance: Doses to lung were found to be higher using TOPAS with respect to analytical calculations which may significantly underestimate dose to the lung, suggesting the use of MC methods for 90Y dosimetry. According to our results, pre-treatment imaging may still be representative of dose to lung in these treatments.

Keywords

90Y-microspheres; TOPAS; internal dosimetry; radionuclides; radioembolization

Introduction

Radioembolization with microspheres containing Yttrium-90 (^{90}Y) is an interventional radiology procedure used to treat both primary and metastatic hepatic malignancies [1]. Patients with discrete and identifiable tumors on imaging studies are normally eligible for this treatment [2]. Typical aims for ^{90}Y treatment include control of metastatic disease [3], downstaging of tumor for resection [4], and primary curative treatment [5]. To do so, ^{90}Y microspheres (either glass [6] or resin [7]) with average diameters between 20 μm and 60 μm are infused into the hepatic arteries so that they circulate across the liver vasculature until they are deposited in end arterioles. The microspheres then emit β particles from ^{90}Y radioisotope decays, imparting energy to surrounding tissues. These emissions have a continuous energy spectrum, with maximum energy of 2.27 MeV (corresponding to a range of 11 mm in soft tissue) and average energy of 0.937 MeV (corresponding to a range of 2.5 mm in soft tissue); and a half-life of 2.66 days [8].

As a radiotherapeutical treatment, the absorbed dose in different structures involved should be considered as the main predictor of outcomes for radioembolization by ^{90}Y [9]. However, the process of radiation dosimetry in these treatments involves several hurdles hampering the determination of dose-response curves [10,11]. First, prior to the administration of the treatment, an angiography of the liver is typically carried out. This allows to map the liver vasculature as well as to check if any aberrant vessels may lead to extrahepatic deposition of activity [12]. Angiography is also useful to guide the localization of a catheter for microsphere infusion into the hepatic arteries for treatment. The most basic version of ^{90}Y

dosimetry consists of a rough conversion of infused activity into absorbed dose taking into account the liver or lung mass [8]. Image-based dosimetry allows a more sophisticated and accurate patient-specific dosimetry, either using SPECT or PET imaging to determine activity distributions [13]. However, image-based dosimetry has its own limitations, as SPECT imaging of ^{90}Y relies on the bremsstrahlung photons emitted by β particles as they are stopped in tissue. This reduces image resolution due to the lack of clear photopeaks. In addition, other corrections for scattering and attenuation are equally hindered [14]. While PET imaging would overcome many of these challenges, it is not routinely used in clinical practice due to reimbursement challenges.

To overcome these problems, microspheres of macroaggregated albumin (MAA) labeled with ^{99m}Tc are first infused as a surrogate for the actual treatment, due to the advantageous properties of ^{99m}Tc for SPECT imaging [15,16]. Although these ^{99m}Tc-MAA microspheres can vary considerably in size, with diameters of up to 150 μm [17], whereas glass ^{90}Y microspheres have a diameter of 15–35 μm and resin microspheres a diameter between 20–60 μm, ^{99m}Tc-MAA microspheres are typically assumed to follow a similar biodistribution [18]. Despite the difference in size, a correlation between tumor dose using ^{99m}Tc-MAA SPECT-based dosimetry and overall survival has been observed [19]. Therefore, these pre-treatment studies are used to assess where activity will presumably be deposited and, in particular, whether a significant portion of it goes to the lung, which is a dose limitant organ due to risk of radiation pneumonitis [20]. Of note, some studies have shown that ^{99m}Tc-MAA intrahepatic distributions can significantly differ from that of ^{90}Y microspheres, particularly for glass microspheres [21].

Assuming that either ^{90}Y-images are of high enough quality or ^{99m}Tc-based pre-treatment images are representative of the actual microsphere distribution, image-based dosimetry can be performed using analytical or Monte Carlo (MC) methods. The analytical method most used in clinical practice is the so-called MIRD formalism or schema which relies on the concept of S-value, i.e., the absorbed dose in a target per unit activity in a source [22]. This approach can be, in turn, broken down into different complexity levels. Originally, the MIRD schema considers a compartmental model in which S-values are defined for organ sources and targets, assuming the activity is uniformly distributed across the organ [23]. For more accuracy, analytical calculations with non-uniform activities can be done by utilizing voxel-wise S-values [24], or the dose-point kernel method [25]. Nonetheless, these methods do not consider heterogeneities within the patient. By contrast, MC techniques inherently include patient heterogeneities and further improve the accuracy of dose calculations, although at a computational cost. One approach to reduce computation time is to use MC codes, such as MCNPX [26] or GATE [27], to obtain radionuclide-specific S-values or dose-point kernels in soft tissue that can be utilized analytically on a patient-by-patient basis [28].

Full MC calculations within the patient require the knowledge of the structural components of a patient and their densities. This information can be obtained from CT images, requiring SPECT-CT or PET-CT hybrid imaging to obtain both the source distribution and patient information. Some tools exist that perform full MC calculations for internal dosimetry such as RAYDOSE [29], VIDA [30], GAMOS [31,32] or GATE [33]. This work analyzes the

dosimetry of 5 patients treated for hepatocellular carcinoma (HCC) with ^{90}Y-microspheres radioembolization in our institutions, estimating with MC accuracy the dose to the tumors, healthy liver and lung. These patients had pre- and post-treatment SPECT-CT studies allowing us to perform cross comparisons of the estimated dose from the ^{99m}Tc-MAA pre-treatment imaging and the actual dose measured with the ^{90}Y post-treatment imaging. MC calculations are carried out with the TOPAS toolkit [34,35], which is a growing framework that wraps up and extends the general purpose code Geant4 [36–38], aiming to make MC simulations user-friendly by removing the need for advanced programming skills.

Methods and Materials

Patient imaging studies

Five patients with HCC treated with ^{90}Y microspheres between February and July 2021 at the Massachusetts General Hospital were selected for this study. Patients received standard of care pre-treatment SPECT-CT imaging, acquired immediately after ^{99m}Tc-MAA administration, and post-treatment SPECT-CT imaging acquired immediately after 90Y microsphere administration. In all cases, angiography was acquired prior to the nuclear medicine study to establish the catheter position for both ^{99m}Tc-MAA and ^{90}Y microsphere infusion. Some differences can be noted among these patients, such as total activity injected, the type of ^{90}Y microspheres used and the final catheter position for the ^{90}Y infusion after pre-treatment mapping of liver vasculature and re-adaptation of the plan. Details are specified in Table 1.

SPECT images were obtained from 64 planar images with a matrix size of 256 × 1024 pixels and uniformity correction. The voxel size of the 3D reconstructed images was 5 mm × 5 mm × 5 mm, the scan length was set to 200 cm and scan speed to 5 cm/min. In all cases, liver and tumors were contoured using the software MiM SurePlan LiverY90 (MiM Software Inc, Cleveland, OH) on the most recent contrast-enhanced cross-sectional imaging of the liver (CT or MR). The type and time between this study and pre-treatment study for each patient are shown in Table 1. Deformable image registrations of the liver were performed between the planning image and both pre- and post-treatment SPECT-CT using Plastimatch, a tool for image processing developed at the Massachusetts General Hospital [39]. Due to large differences in patient positioning, a mask with high contrast was added as an additional shell of 5 mm surrounding the liver structures contoured using MiM. This mask was only used for the image registration, not for dose calculations. Deformable image registration was then performed using the B-splines algorithm, optimizing the mean square error as the cost function. This procedure allowed for a direct propagation of the relative position of tumors within the liver from one study to another.

Dose calculation using voxel-wise S-values (MIRD schema)

Using the intensity (counts) of both pre- and post-treatment SPECT images, we performed analytical calculations using voxel-wise S-values in soft tissue for ^{90}Y. S-values were taken from the database published by Lanconelli et al. [40], corresponding to our voxel size with 5 mm resolution. For this application, $S(d \leftarrow i)$ is the S-value for a voxel at a distance d from i and it is given for the total number of voxels N according to their distance d to the ith voxel.

Then, $S(d \leftarrow i)$ specifies the absorbed dose by the voxel at a distance d per unit activity in the voxel i, $A_i(t)$. Therefore, the dose rate at a voxel $k = i \pm d$ (i.e., located at a distance d from the voxel i) at the time t is given by

$$\dot{D}_{k=i\pm d}(t) = \sum_{i=1}^{N} A_i(t) S(d \leftarrow i) \tag{1}$$

where N represents the total number of voxels and j represents the distance between the voxel k and the voxel i. Under this formalism, S-values are assumed to be constant along time, so that if $\hat{A} = \int A(t)\mathrm{d}t$ is the cumulative activity, the total absorbed dose by the voxel k is given by

$$D_k = \int_{t_0}^{\infty} \dot{D}_k(t)\mathrm{d}t = \sum_{i=1}^{N} \int_{t_0}^{\infty} A_i(t)\mathrm{d}t \; S(d \leftarrow i) \tag{2}$$

As the ^{90}Y microspheres are used to embolize vessels, it is assumed here that all the activity is delivered locally, i.e., there is neither biological washout nor activity redistribution after imaging. In that case, equation (2) can be rewritten as

$$D_k = \sum_{i=1}^{N} \frac{A_{0,i}}{\lambda} S(d \leftarrow i) \tag{3}$$

where $A_{0,i}$ is the initial activity at the voxel i and $\lambda = 0.258$ days^{-1} is the decay constant for ^{90}Y emissions. A normalization condition is introduced as $A_0 = \sum_i A_{0,i}$, where A_0 is the total activity infused, assuming all the activity administered is contained within the SPECT image. In this work we used this condition to report total absorbed dose per unit activity administered, D/A_0. Once dose was calculated using the SPECT image, a 3D interpolation process was performed to obtain doses in CT-based matrixes. The interpolation method used the inverse of the distance between each node in the CT matrix and the 8 closest nodes in the SPECT matrix to weight the contribution from each SPECT matrix node. This application has also been developed for this study and it is publicly available at https://github.com/mghro/MIRDCalculation. Doses were scaled to consider only the activity within the patient, using the threshold HU > −900 in the CT studies to determine voxels belonging to the patient anatomy. This threshold was determined after visual inspection to make sure air outside the patient was not included but lungs were.

Dose calculation using TOPAS

TOPAS [34,35] is a wrapped and extended version of the Geant4 [36–38] Monte Carlo toolkit specifically focused on medical physics. While TOPAS makes use of the broadly validated physics models and the architecture of Geant4, multiple tools have been developed by the TOPAS community aiming at simplifying MC simulations for medical physicists and radiation oncologists without expertise on coding. TOPAS uses *geometry components* to specify shapes and materials, *particle sources and generators* to initiate radiation, *modular physics lists* to specify what physics interactions and cross sections are considered and

scorers to tally and measure quantities of interest. A user can create a simulation in TOPAS with a simple text file following a syntax based on parameters. For instance, some ready-to-use tools are geometrical shapes and complex nested structures, scoring of radiotherapy relevant quantities, and time features, i.e., the ability of handling motions of all components of the simulation. TOPAS interprets DICOM files, such as CT scans, as well as contours or dose distributions stored as DICOM-RT standard. A DICOM-based CT scan is generated as a geometry component in TOPAS, following a voxelized geometry with twofold purpose: assigning a given material to each voxel and serving as the reference to score absorbed dose. For the former, TOPAS uses the method proposed by Schneider et al. [41] and the correction proposed by Paganetti et al. [42] to associate Hounsfield Units and material composition, employing 25 different tissue-based materials and densities.

We developed two new classes in TOPAS (v3.7) to read nuclear medicine DICOM files, such as SPECT or PET images. The first one is a geometry component, *TsDicomActivityMap*, which serves to position the SPECT image, i.e., activity map, relative to the patient geometrical object, created from the CT images. Positions for voxels with counts higher than a given threshold in the nuclear medicine image (0 for this work) are then recorded. The second one is a particle source and generator, *TsGeneratorActivityMap*, which generates the particles emitted by radionuclides. To simulate one history, first a voxel from *TsDicomActivityMap* is selected with a probability proportional to its number of counts. Then, the position of the emission is uniformly sampled within the voxel, and a direction is isotropically sampled. Finally, a given emission is selected for the considered radionuclide, i.e., particle and energy of emission. For ^{90}Y, only electrons are considered following the emission spectrum taken from the RADAR database [43]. Figure 1 shows a diagram of the process followed in TOPAS for the implementation of internal dosimetry calculations. A simulation is then run in TOPAS by using a simple parameter text file, for which the user only has to specify the radionuclide employed, the path of the CT and NM DICOM files, the number of decays to be simulated and the physics lists to be employed. The internal dosimetry feature will be publicly available for the TOPAS community in future releases of the code.

TOPAS can employ any of the reference physics lists already contained in the Geant4 toolkit. Users can specify what models are used to represent different physical processes as a trade-off between accuracy and speed depending on the application. The default electromagnetic (EM) physics constructor of Geant4 uses the Coulomb model for single scattering and the Urban model for multiple scattering of electrons with kinetic energy up to 100 MeV [44]. However, option 4 of the EM physics constructor of Geant4 offers the highest accuracy for electron tracking, using the Goudsmit-Saunderson model for multiple scattering for up to 100-MeV electrons and more detailed models for ionization and bremsstrahlung for low-energy electrons [38]. In order to test the validity of the default EM physics constructor for our application, we calculated the S values for ^{90}Y emissions in soft tissue, as defined by the ICRU Report 44 [45], using TOPAS with both default and ‘option 4’ EM physics constructors. Our results were compared to those obtained by Lanconelli et al. [40].

Using the default EM physics constructor, we simulated 10^7 histories for each patient, which represents a total initial activity of A_0 = 10 MBq. Results provided by TOPAS simulations in this context represent the dose rate per 10 MBq of activity at the time of imaging, $\dot{D}_0/10\,\text{MBq}$. In order to calculate the total absorbed dose at $t \rightarrow \infty$, a similar operation as done in equations (2–3) is performed as:

$$\frac{D}{A_0} = \frac{1}{A_0}\int_{t_0}^{\infty} \dot{D}(t)\mathrm{d}t = \frac{\dot{D}_0/10\,\text{MBq}}{\lambda} \quad (4)$$

Results

S values for ^{90}Y were calculated using TOPAS with both the standard and ‘option 4’ EM physics constructors for three voxel sizes, 2.21 mm, 5 mm and 9.28 mm, so that they can be compared to three of the datasets from Lanconelli et al. [40]. Figure 2 shows the comparison between these values.

Differences between default and ‘option4’ physics in TOPAS were within 1.5% for the self-irradiated voxel (i.e., distance = 0) in al cases, for all voxel sizes. Maximum differences for the smallest voxel size scaled up to −65% around 10 mm, which represents the maximum range for the electrons emitted under the continuous slow-down approximation (CSDA). Relative differences at about this distance increased with larger voxels, although the absolute S values also decreased for larger voxels. Of note, while the simulation of 10^7 emissions took 30 min on average for the default EM physics constructor using a single iMac (3.5 GHz processor, 32 GB memory), this time went up to 42 h for the ‘option 4’ EM physics constructor, i.e., about 85 times longer. Database values from Lanconelli et al. [40] showed an approximate 30% decreased dose to the self-irradiated voxel, which seemed to be compensated by increased doses in immediately surrounding voxels. These differences may be due to discrepancies in both the physics models, the definition of soft tissue employed or geometrical specifications. Statistical uncertainties in the doses for the 5 mm-voxel size ranged from 0.006% for the self-irradiated voxel to 7% at 5 voxels distance (i.e., 25 mm). Using 10 MBq, for patient calculations in high-dose regions, where voxels emit between 0.001% and 0.01% of the total activity, uncertainty to the self-absorbed dose was estimated at around 0.9%. Uncertainties at low-dose regions are greater.

Figure 3 shows the SPECT-CT images for pre-treatment studies for each patient, as well as MIRD schema and TOPAS calculations of absorbed dose per unit activity administered.

By contrast, Figure 4 shows SPECT-CT images and dose calculations according to both methods for the post-treatment studies in approximately the same axial planes.

Differences in lung doses using TOPAS and MIRD are illustrated on Figure 5, which shows an axial slice of the pre-treatment CT study for patient 1. Similar results are observed for the other patients as well as in post-treatment studies.

Figure 6 shows a comparison of the cumulative dose-volume histograms (DVHs) (per unit activity) obtained in tumors in both hemi-livers (left tumors and right tumors), right lung and

the entire liver when using TOPAS and MIRD dosimetric methods. The actual ^{90}Y SPECT-CT studies were used for this comparison. As expected, dose to lung was underestimated using analytical methods due to the lack of consideration of tissue heterogeneities. For the rest of structures considered, no clear trend in differences between MC and MIRD schema was observed.

Additionally, Figure 7 shows the DVHs calculated with MC techniques (TOPAS) for pre- and post-treatment images to illustrate the possibility of using pre-treatment imaging to assess the actual dose distributions with ^{90}Y microspheres.

Figure 8 summarizes results for all patients in terms of mean dose to the considered structures, i.e., the whole liver, right and left tumors and right lung. Differences between analytical and Monte Carlo calculations are stressed in the top panels, where a significant difference is shown for lung, but good agreement is found for liver and tumors. The bottom panels illustrate the discrepancies between pre- and post-treatment imaging-based dosimetry.

Discussion

Two main points have been addressed in this work: (a) what are the differences between MC and analytical methods to calculate dosimetry for ^{90}Y-based radioembolization -particularly for lung-; and (b) how do pre- and post-treatment image-based dosimetry differ. Both have been previously studied: for example, Auditore et al. [31] evaluated the differences between GAMOS and a convolution kernel method, although not for lung shunt. Allred et al. [46] evaluated differences between pre- and post-treatment SPECT-CT images using a phantom instead of patient data. This work combines all these elements: we provide MC-accurate quantitative data for tumor, healthy tissue and lung dosimetry comparing pre- and post-treatment SPECT-CT. TOPAS has been used for the MC calculations with the standard EM physics constructor of Geant4 rather than the more accurate ‘option4’, provided that differences in calculation times were up to two orders of magnitude higher and dose differences were small for the major portion of the absorbed dose (concentrated on the self-irradiated and adjacent voxels). As a toolkit with multiple useful developments for medical physics, TOPAS incorporates a method to classify HU from a CT study into 25 different tissue-like materials following the approach by Schneider et al. [41], in contrast with other MC implementations in which only 4–5 materials are used [31,47]. Differences in mass densities and materials have been recently shown to be important for lung dose [48].

Differences for (a) can be seen in the dose distribution overlaid on the CT images in Figures 3–5 and in terms of accumulated dose per unit activity in Figure 6. As analytical methods typically do not consider differences in tissue composition, they were expected to underestimate dose to lung due to its low density. Our results confirm this premise, showing a significant increase in doses to lung for all patients when MC calculations are used. In particular, differences of mean calculated dose to the lung differed between methods from 1.2 Gy/GBq to 6.3 Gy/GBq (or 153% to 231% in relative values), with an average difference of 3.4 Gy/GBq (or 168% in relative values). This result is in line with previous studies comparing soft tissue kernels without correcting by density with calculations using the MC DOSXYZnrc code [47]. In fact, this may carry clinical consequences, as one of the main

limiting factors for ^{90}Y treatment eligibility is the lung shunt fraction (LSF), i.e., the fraction of activity deposited within the lungs. LSF is typically evaluated directly on SPECT imaging or using analytical methods to compute dose. Dose calculation guidelines limit the dose received after a single ^{90}Y treatment to 30 Gy, and the cumulative total dose to 50 Gy. Our results show that the actual LSF may be underestimated if MC techniques are not used. This finding suggests that the recommended pulmonary dose threshold may be more commonly exceeded than realized. Consequently, since the reported side effects with the currently employed calculation scheme are not exceeding expectation, the actual tolerable LSF limits may be higher for ^{90}Y treatments than the limit used in current clinical practice. However, due to respiratory motion and the long time required for SPECT acquisitions, the actual biodistribution of activity in lungs is likely blurred or averaged along the patient motion, so that the voxel-based calculations might be affected. This effect can be particularly important near the lung-liver interface in the instance that high activity is concentrated over that area of the liver. These factors complicate lung dosimetry and as recently acknowledged by the European Association of Nuclear Medicine (EANM) Dosimetry Committee, determining limits for lung dose remain a completely open problem [49].

Additionally, Patient 5 showed significant differences in doses to the tumors in the right side of the liver, up to 21% higher when using MC calculations. As shown in Figure 4, uptake of patient 5 showed a pronounced peak in a small region near the right tumors on the right (inferior) part of the liver. Such a pattern, together with the uncertainties due to the interpolation of the dose grid, might introduce partial volume effects when using analytical methods using voxel-wise S-values, which can result in an underestimation of the dose in the contiguous voxels as shown in patient 5. However, as shown in Figure 2, S-values from the Lanconelli et al. [40] database underestimate the dose to the source voxel with respect to TOPAS, which also contributes to enhanced differences when activity peaks in single voxels. In situations with activity uptake distributed over larger regions, TOPAS and MIRD schema-based calculations were within comparable accuracy, as partial volume effects are not observed and differences in the self-irradiated voxels between TOPAS and Lanconelli et al. [40] are compensated by the contributions to the dose from activity in the surrounding voxels. For instance, mean doses to the liver did not exceed 1.4 Gy/GBq (or 13% in relative values) for any patient, with an average difference of 0.14 Gy/GBq (or 2.6% in relative values) between MC and MIRD-schema calculations.

As for point (b) pre- and post-treatment image-based dosimetry, significant differences were observed between the dose distribution predicted by the pre-treatment images and the actual dose distribution calculated upon ^{90}Y images, as illustrated in the bottom panels of Figure 8. For example, the D50 in the target was up to a factor 4 (for patient 4) higher when using pre-treatment images. This is likely due to the change of the catheter position after assessing pre-treatment images (see Table 1), which significantly changes the pathways of the infused activity through the vasculature. In this specific instance, a left-sided tumor included in the ^{99m}Tc-MAA injection was not treated with ^{90}Y during this session. Overall, these results also demonstrate the necessity of using voxel-based dosimetry instead of compartmental models for ^{90}Y-microsphere radioembolization as distributions of activity are far from being uniform in liver sub-regions [50].

Other factors also contribute to this disparity: ^{99m}Tc-MAA microspheres are inherently different from ^{90}Y microspheres. This may result in the two microsphere types being preferentially deposited in different vessels [51]. Note that differences in doses to tumors are notable for all patients, as shown in Figure 7, as differences in biodistributions of activity from pre- to post-treatment images are mainly due to changes on the catheter position within the liver. However, doses to the lung evaluated in pre- and post-treatment images showed a good agreement, as observed in the phantom study by Allred et al. [46]. In fact, as shown in Figure 8, using analytical methods instead of MC techniques produced greater discrepancies than using pre-treatment dosimetry in the estimation of the dose to the lung. This seems to support the use of pre-treatment imaging to estimate LSF as extrahepatic shunts are probably not as affected as intrahepatic biodistribution by changes in delivery positions within the liver.

In addition to studying dosimetry for ^{90}Y microsphere treatments, this work also presents TOPAS as a powerful MC tool to perform internal dosimetry for radiopharmaceutical treatments. Besides providing access to complex MC calculations to nuclear medicine and medical physics users without expertise in programming, a growing body of extensions of TOPAS are being developed in potential relevant fields for internal dosimetry. Examples of these are the microdosimetry extension [52], the brachytherapy toolkit [53] or the nano-scale radiobiological project TOPAS-nBio [54]. Our implementation of a SPECT-based source in TOPAS assumes a uniform activity within a given voxel but the electron tracks are still simulated at a smaller scale, sampled by default randomly within the voxel, which can be seen by the granularity of the dose distributions with TOPAS in Figures 3 and 4. Note that any other assumption or model of intra-voxel activity is also implementable using TOPAS. Interestingly, the versatility of the TOPAS architecture allows for non-uniform activity distributions, as well as potential breakdowns of a voxel (macroscopic scale) into smaller structures like those developed in the TOPAS-nBio project. Although in this work we have employed ^{90}Y microspheres which are assumed to remain immobile, internal dosimetry for other radiopharmaceutical treatments involves the time evolution of the activity administered. Time features are already integrated in TOPAS, which can be of great help in these situations. The current version presented in this work is, however, limited to dose calculation from a static SPECT image. The development of more flexible internal dosimetry tools is a potential future workline for the TOPAS team.

Conclusions

TOPAS results showed comparable doses to the entire liver and tumors, but a significantly greater dose to lungs than predicted by the voxel-level MIRD. This suggests the importance of using MC techniques to assess lung shunt fraction in radiopharmaceutical treatments. Dosimetry predicted by pre-treatment imaging was compared to that from post-treatment imaging, showing significant intrahepatic differences due to changes in the delivery position within the liver. However, dose to lung due to lung shunt fraction was comparable for pre- and post-treatment imaging. Therefore, pre-treatment images were found to be potentially useful for estimating dose limits for organs at risk (e.g., lung).

Funding:

This work was in part supported by the National Institutes of Health/National Cancer Institute (NIH/NCI grant no. U24 CA 215123: “The TOPAS Tool for Particle Simulation, a Monte Carlo Simulation Tool for Physics, Biology and Clinical Research”). Eric Wehrenberg-Klee is supported by the NIH/NCI grant K08 CA 245257. Alejandro Bertolet is supported by the NIH/NCI grant no. K99 CA267560

References

1. Kim SP, Cohalan C, Kopek N, Enger SA. A guide to 90Y radioembolization and its dosimetry. Phys Medica. Elsevier; 2019;68:132–45.
2. Wehrenberg-Klee E, Gandhi RT, Ganguli S. Patient Selection and Clinical Outcomes of Y90 in Hepatocellular Carcinoma. Tech Vasc Interv Radiol. Elsevier Inc.; 2019;22:70–3. [PubMed: 31079713]
3. Gulec SA, Mesoloras G, Dezarn WA, McNeillie P, Kennedy AS. Safety and efficacy of Y-90 microsphere treatment in patients with primary and metastatic liver cancer: The tumor selectivity of the treatment as a function of tumor to liver flow ratio. J Transl Med. 2007;5:1–9. [PubMed: 17201925]
4. Lau WY, Kennedy AS, Kim YH, Lai HK, Lee RC, Leung TWT, et al. Patient selection and activity planning guide for selective internal radiotherapy with yttrium-90 resin microspheres. Int J Radiat Oncol Biol Phys. 2012;82:401–7. [PubMed: 20950954]
5. Salem R, Johnson GE, Kim E, Riaz A, Bishay V, Boucher E, et al. Yttrium-90 Radioembolization for the Treatment of Solitary, Unresectable HCC: The LEGACY Study. Hepatology. 2021;0:1–11.
6. Salem R, Lewandowski R, Roberts C, Goin J, Thurston K, Abouljoud M, et al. Use of Yttrium-90 Glass Microspheres (TheraSphere) for the Treatment of Unresectable Hepatocellular Carcinoma in Patients with Portal Vein Thrombosis. J Vasc Interv Radiol. 2004;15:335–45. [PubMed: 15064336]
7. Wang EA, Stein JP, Bellavia RJ, Broadwell SR. Treatment options for unresectable HCC with a focus on SIRT with Yttrium-90 resin microspheres. Int J Clin Pract. 2017;71:1–15.
8. Gulec SA, Mesoloras G, Stabin M. Dosimetric techniques in 90Y-microsphere therapy of liver cancer: The MIRD equations for dose calculations. J Nucl Med. 2006;47:1209–11. [PubMed: 16818957]
9. d’Abadie P, Walrand S, Hesse M, Annet L, Borbath I, van den Eynde M, et al. Prediction of tumor response and patient outcome after radioembolization of hepatocellular carcinoma using 90Y-PET-computed tomography dosimetry. Nucl Med Commun. 2021;42:747–54. [PubMed: 33741864]
10. Srinivas SM, Natarajan N, Kuroiwa J, Gallagher S, Nasr E, Shah SN, et al. Determination of radiation absorbed dose to primary liver tumors and normal liver tissue using post radioembolization 90Y PET. Front Oncol. 2014;4:1–12. [PubMed: 24478982]
11. Chansanti O, Jahangiri Y, Matsui Y, Adachi A, Geeratikun Y, Kaufman JA, et al. Tumor Dose Response in Yttrium-90 Resin Microsphere Embolization for Neuroendocrine Liver Metastases: A Tumor-Specific Analysis with Dose Estimation Using SPECT-CT. J Vasc Interv Radiol. SIR; 2017;28:1528–35.
12. van den Hoven AF, Smits MLJ, de Keizer B, van Leeuwen MS, van den Bosch MAAJ, Lam MGEH. Identifying Aberrant Hepatic Arteries Prior to Intra-arterial Radioembolization. Cardiovasc Intervent Radiol. 2014;37:1482–93. [PubMed: 24469409]
13. O’ Doherty J A review of 3D image-based dosimetry, technical considerations and emerging perspectives in 90Y microsphere therapy. J Diagnostic Imaging Ther. 2015;2:1–34.
14. Kubik A, Budzyńska A, Kacperski K, MacIak M, Kuć M, Piasecki P, et al. Evaluation of qualitative and quantitative data of Y-90 imaging in SPECT/CT and PET/CT phantom studies. PLoS One. 2021;16:1–16.
15. Campbell JM, Wong CO, Muzik O, Marples B, Joiner M, Burmeister J. Early Dose Response to Yttrium-90 Microsphere Treatment of Metastatic Liver Cancer by a Patient-Specific Method Using Single Photon Emission Computed Tomography and Positron Emission Tomography. Int J Radiat Oncol Biol Phys. 2009;74:313–20. [PubMed: 19362251]

16. Kao YH, Magsombol BM, Toh Y, Tay KH, Chow PKH, Goh ASW, et al. Personalized predictive lung dosimetry by technetium-99m macroaggregated albumin SPECT/CT for yttrium-90 radioembolization. EJNMMI Res. 2014;4:1–12. [PubMed: 24382020]
17. Dezarn WA, Cessna JT, Dewerd LA, Feng W, Gates VL, Halama J, et al. Recommendations of the American Association of Physicists in Medicine on dosimetry, imaging, and quality assurance procedures for 90Y microsphere brachytherapy in the treatment of hepatic malignancies. Med Phys. 2011;38:4824–45. [PubMed: 21928655]
18. Kennedy A, Nag S, Salem R, Murthy R, McEwan AJ, Nutting C, et al. Recommendations for Radioembolization of Hepatic Malignancies Using Yttrium-90 Microsphere Brachytherapy: A Consensus Panel Report from the Radioembolization Brachytherapy Oncology Consortium. Int J Radiat Oncol Biol Phys. 2007;68:13–23. [PubMed: 17448867]
19. Garin E, Rolland Y, Laffont S, Edeline J. Clinical impact of 99mTc-MAA SPECT/CT-based dosimetry in the radioembolization of liver malignancies with 90Y-loaded microspheres. Eur J Nucl Med Mol Imaging. 2016;43:559–75. [PubMed: 26338177]
20. Wright CL, Werner JD, Tran JM, Gates VL, Rikabi AA, Shah MH, et al. Radiation pneumonitis following yttrium-90 radioembolization: Case report and literature review. J Vasc Interv Radiol. Elsevier Inc.; 2012;23:669–74. [PubMed: 22525023]
21. Wondergem M, Smits MLJ, Elschot M, De Jong HWAM, Verkooijen HM, Van Den Bosch MAAJ, et al. 99mTc-macroaggregated albumin poorly predicts the intrahepatic distribution of 90Y resin microspheres in hepatic radioembolization. J Nucl Med. 2013;54:1294–301. [PubMed: 23749996]
22. Howell RW. The MIRD Schema: From organ to cellular dimensions. J Nucl Med. 1994;35:531–3. [PubMed: 8113909]
23. Snyder WS, Ford MR, Warner GG, Watson SB. MIRD Pamphlet No. 11: Absorbed dose per unit cumulate activity for selected radionuclides and organs New York, NY; 1975.
24. Bolch WE, Bouchet LG, Robertson JS, Wessels BW, Siegel JA, Howell RW, et al. MIRD pamphlet no. 17: The dosimetry of nonuniform activity distributions - Radionuclide S values at the voxel level. J Nucl Med. 1999;40. [PubMed: 9935054]
25. Giap HB, Macey DJ, Bayouth JE, Boyer AL. Validation of a dose-point kernel convolution technique for internal dosimetry. Phys Med Biol. 1995;40:365–81. [PubMed: 7732068]
26. Forster RA, Godfrey TNK. MCNP - a general Monte Carlo code for neutron and photon transport. Los Alamos, NM; 1985.
27. Jan S, Benoit D, Becheva E, Lin H, Chuang K, Lin Y, et al. GATE : a simulation toolkit for PET and SPECT. Phys Med Biol. 2004;49:4543–4561. [PubMed: 15552416]
28. Villoing D, Marcatili S, Garcia MP, Bardiès M. Internal dosimetry with the Monte Carlo code GATE: Validation using the ICRP/ICRU female reference computational model. Phys Med Biol. 2017;62:1885–904. [PubMed: 28182580]
29. Marcatili S, Pettinato C, Daniels S, Lewis G, Edwards P, Fanti S, et al. Development and validation of RAYDOSE: A Geant4-based application for molecular radiotherapy. Phys Med Biol. 2013;58:2491–508. [PubMed: 23514870]
30. Kost SD, Dewaraja YK, Abramson RG, Stabin MG. VIDA: A voxel-based dosimetry method for targeted radionuclide therapy using Geant4. Cancer Biother Radiopharm. 2015;30:16–26. [PubMed: 25594357]
31. Auditore L, Amato E, Boughdad S, Meyer M, Testart N, Cicone F, et al. Monte Carlo 90Y PET/CT dosimetry of unexpected focal radiation-induced lung damage after hepatic radioembolisation. Phys Med Biol. 2020;65.
32. Amato E, Auditore L, Italiano A, Pistone D, Arce P, Campenn A, et al. Full Monte Carlo internal dosimetry in nuclear medicine by means of GAMOS. J Phys Conf Ser. 2020;1561.
33. Neira S, Guiu-Souto J, Díaz-Botana P, Pais P, Fernández C, Pubul V, et al. Quantification of internal dosimetry in PET patients: individualized Monte Carlo vs generic phantom-based calculations. Med Phys. 2020;47:4574–88. [PubMed: 32569389]
34. Perl J, Shin J, Schumann J, Faddegon B, Paganetti H. TOPAS: An innovative proton Monte Carlo platform for research. Med Phys. 2012;39:6818–37. [PubMed: 23127075]

35. Faddegon B, Ramos-Méndez J, Schuemann J, McNamara A, Shin J, Perl J, et al. The TOPAS tool for particle simulation, a Monte Carlo simulation tool for physics, biology and clinical research. Phys Medica. Elsevier; 2020;72:114–21.
36. Agostinelli S, Allison J, Amako K, Apostolakis J, Araujo H, Arce P, et al. Geant4—a simulation toolkit. Nucl Instruments Methods Phys Res Sect A Accel Spectrometers, Detect Assoc Equip. 2003;506:250–303.
37. Allison J, Amako K, Apostolakis J, Araujo H, Arce Dubois P, Asai M, et al. Geant4 developments and applications. IEEE Trans Nucl Sci. 2006;53:270–8.
38. Allison J, Amako K, Apostolakis J, Arce P, Asai M, Aso T, et al. Recent developments in Geant4. Nucl Instruments Methods Phys Res Sect A Accel Spectrometers, Detect Assoc Equip. North-Holland; 2016;835:186–225.
39. Sharp G, Li R, Wolfgang J, Chen G, Peroni M, Spadea MF, et al. Plastimatch: an open source software suite for radiotherapy image processing. Proc XVI'th Int Conf use Comput Radiother. 2010;
40. Lanconelli N, Pacilio M, Meo, Botta F, Dia A Di, Aroche LAT, et al. A free database of radionuclide voxel S values for the dosimetry of nonuniform activity distributions. Phys Med Biol. 2012;57:517–33. [PubMed: 22217735]
41. Schneider W, Bortfeld T, Schlegel W. Correlation between CT numbers and tissue parameters needed for Monte Carlo simulations of clinical dose distributions. Phys Med Biol. 2000;45:459–78. [PubMed: 10701515]
42. Paganetti H, Jiang H, Parodi K, Slopsema R, Engelsman M. Clinical implementation of full Monte Carlo dose calculation in proton beam therapy. Phys Med Biol. 2008;53:4825–53. [PubMed: 18701772]
43. Stabin MG, Da Luz LCQP. Decay data for internal and external dose assessment. Health Phys. 2002;83:471–5. [PubMed: 12240721]
44. Ivanchenko V, Apostolakis J, Bagulya A, Abdelouahed H Ben, Black R, Bogdanov A, et al. Recent Improvements in Geant4 Electromagnetic Physics Models and Interfaces. Prog Nucl Sci Technol. 2011;2:898–903.
45. White DR, Booz J, Griffith RV., Spokas JJ, Wilson IJ. ICRU Report 44, Tissue Substitutes in Radiation Dosimetry and Measurements. J Int Comm Radiat Units Meas. 1989;23:1–189.
46. Allred JD, Niedbala J, Mikell JK, Owen D, Frey KA, Dewaraja YK. The value of 99mTc-MAA SPECT/CT for lung shunt estimation in 90Y radioembolization: a phantom and patient study. EJNMMI Res. 2018;8:50. [PubMed: 29904808]
47. Mikell JK, Mahvash A, Siman W, Mourtada F, Kappadath SC. Comparing voxel-based absorbed dosimetry methods in tumors, liver, lung, and at the liver-lung interface for 90Y microsphere selective internal radiation therapy. EJNMMI Phys [Internet]. EJNMMI Physics; 2015;2:1–14. Available from: 10.1186/s40658-015-0119-y [PubMed: 26501803]
48. Kim SP, Juneau D, Cohalan C, Enger SA. Standardizing SPECT/CT dosimetry following radioembolization with yttrium-90 microspheres. EJNMMI Phys [Internet]. Springer International Publishing; 2021;8:71. Available from: 10.1186/s40658-021-00413-3
49. Chiesa C, Sjogreen-Gleisner K, Walrand S, Strigari L, Flux G, Gear J, et al. EANM Dosimetry Committee Series on Standard Operational Procedures: a unified methodology for 99mTc-MAA pre- and 90Y peri-therapy dosimetry in liver radioembolization with 90Y microspheres. EJNMMI Phys. EJNMMI Physics; 2021;8:77. [PubMed: 34767102]
50. Hashikin NAA, Yeong CH, Guatelli S, Abdullah BJJ, Ng KH, Malaroda A, et al. Systematic investigation on the validity of partition model dosimetry for 90Y radioembolization using Monte Carlo simulation. Phys Med Biol. IOP Publishing; 2017;62:7342–56. [PubMed: 28686171]
51. Van De Wiele C, Maes A, Brugman E, D'Asseler Y, De Spiegeleer B, Mees G, et al. SIRT of liver metastases: Physiological and pathophysiological considerations. Eur J Nucl Med Mol Imaging. 2012;39:1646–55. [PubMed: 22801733]
52. Zhu H, Chen Y, Sung W, McNamara AL, Tran LT, Burigo LN, et al. The microdosimetric extension in TOPAS: Development and comparison with published data. Phys Med Biol. IOP Publishing; 2019;64:0–15.

53. Berumen F, Ma Y, Ramos-Méndez J, Perl J, Beaulieu L. Validation of the TOPAS Monte Carlo toolkit for HDR brachytherapy simulations. Brachytherapy. 2021;20:911–21. [PubMed: 33896732]

54. Schuemann J, McNamara AL, Ramos-Méndez J, Perl J, Held KD, Paganetti H, et al. TOPAS-nBio: An Extension to the TOPAS Simulation Toolkit for Cellular and Sub-cellular Radiobiology. Radiat Res. 2019;191:125–38. [PubMed: 30609382]

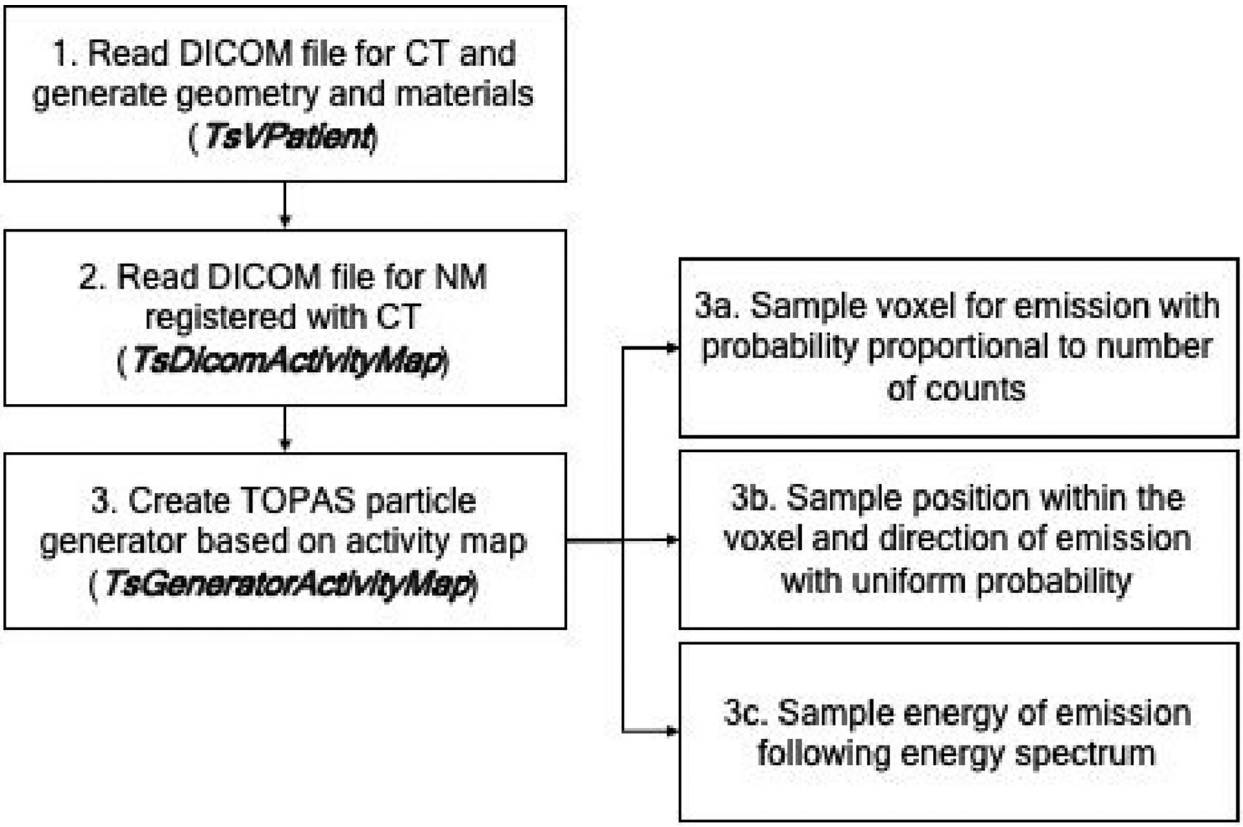

Figure 1.
Schematic representation of the workflow in TOPAS to produce internal dosimetry calculations using SPECT-CT or PET-CT hybrid studies.

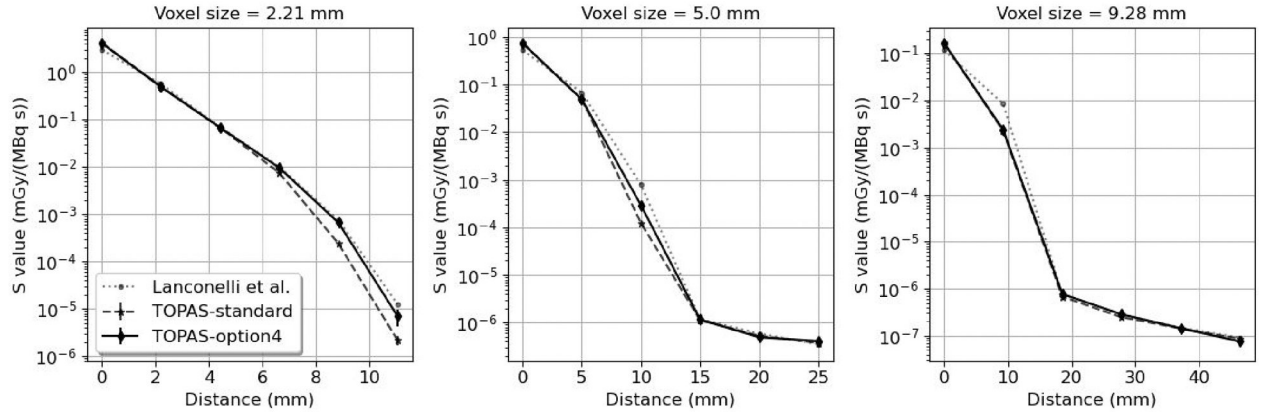

Figure 2.

Upper panels show voxel-wise S-values calculated using two EM physics constructors in TOPAS: ‘standard’ and ‘option4’, compared to the values given in the database from Lanconelli et al. [40], for three voxel sizes (2.21 mm, 5.0 mm and 9.28 mm). Lower panels show relative differences between S-values with respect to the TOPAS ‘option4’ for the same voxel sizes.

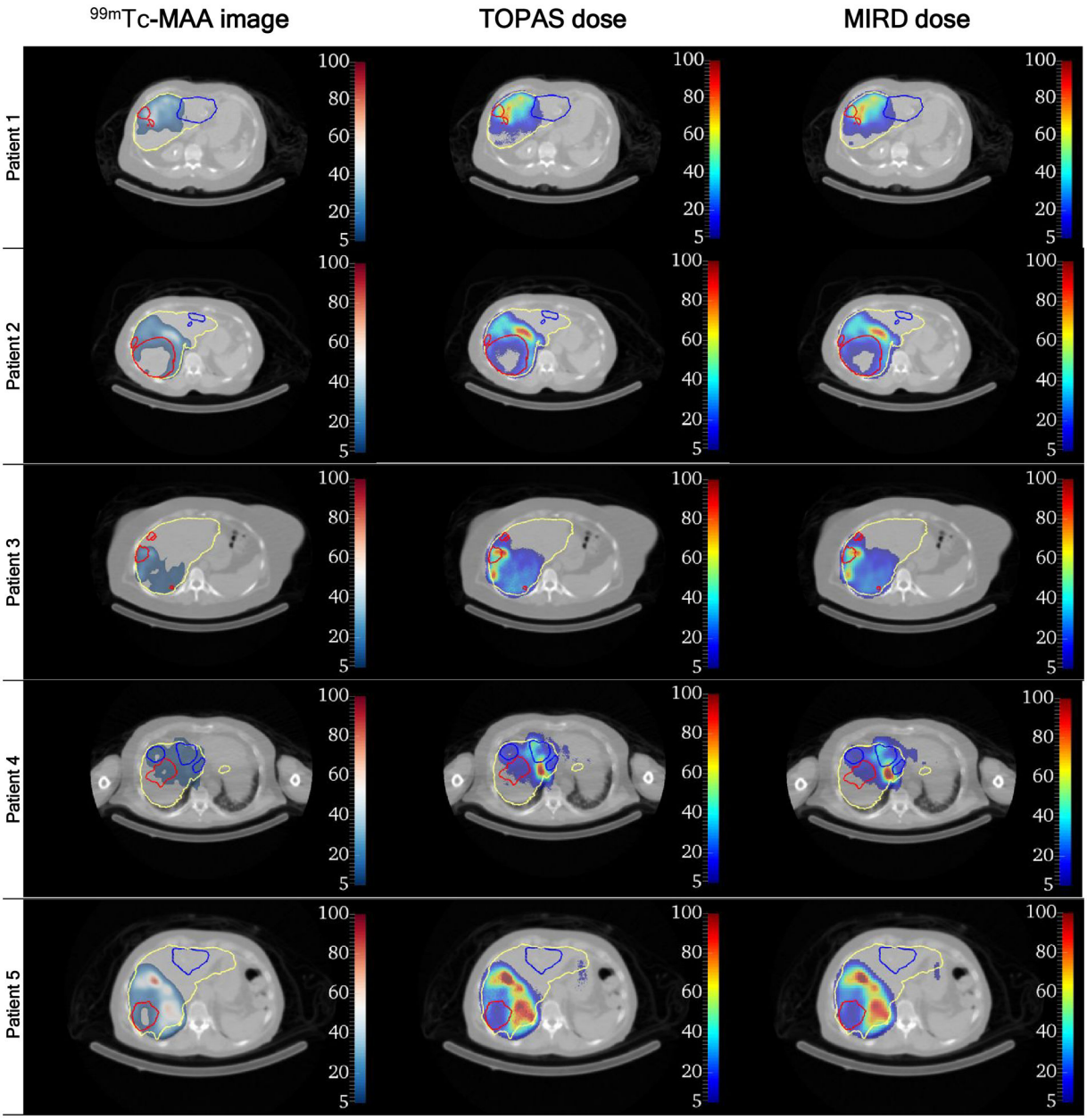

Figure 3.

Distributions of activity (*left*) and doses calculated via TOPAS (*middle*) and the MIRD schema (*right*) in an axial plane for each patient, after the injection of ^{99m}Tc-MAA. The entire liver is represented by a yellow contour, tumors on the right hemi-liver by red contours and tumors on the left hemi-liver by blue contours. Color maps indicate the percentage of counts in a voxel with respect to the maximum number of counts for the SPECT image, and Gy/GBq for the TOPAS and MIRD schema calculations. Thresholds for visualization are set to 5% of the maximum number of counts for the SPECT-CT, and 5 Gy/GBq for the dose visualizations. Activity distributions are interpolated and smoothened by the 3DSlicer viewer.

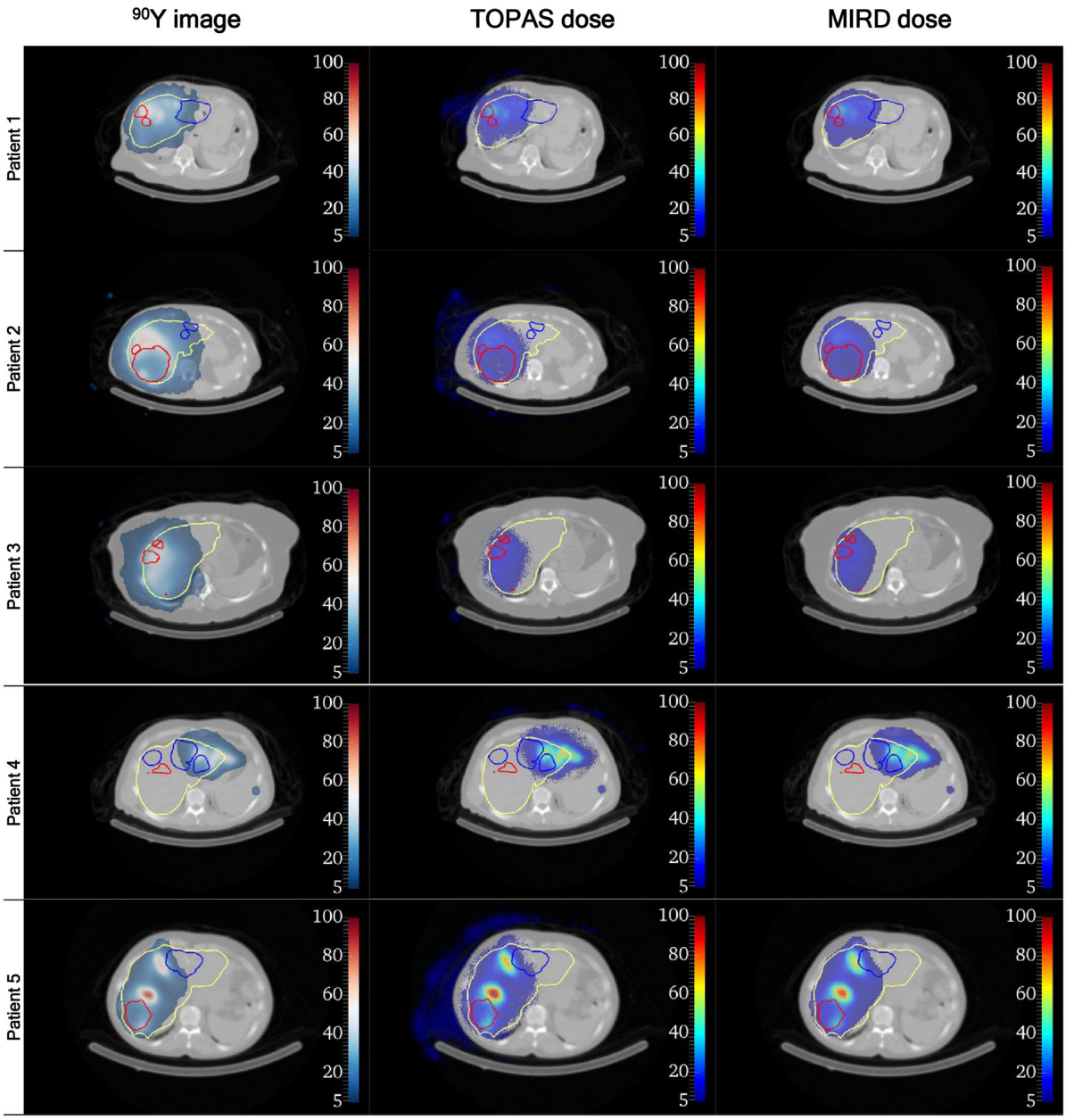

Figure 4.

Distributions of activity (*left*) and doses calculated via TOPAS (*middle*) and the MIRD schema (*right*) in an axial plane for each patient, after SPECT imaging of the ^{90}Y microspheres used as treatment. The entire liver is represented by a yellow contour, tumors on the right hemi-liver by red contours and tumors on the left hemi-liver by blue contours. Color maps indicate the percentage of counts in a voxel with respect to the maximum number of counts for the SPECT image, and Gy/GBq for the TOPAS and MIRD schema calculations. Thresholds for visualization are set to 5% of the maximum number of counts for the SPECT-CT, and 5 Gy/GBq for the dose visualizations. Activity distributions are interpolated and smoothened by the 3DSlicer visualizator.

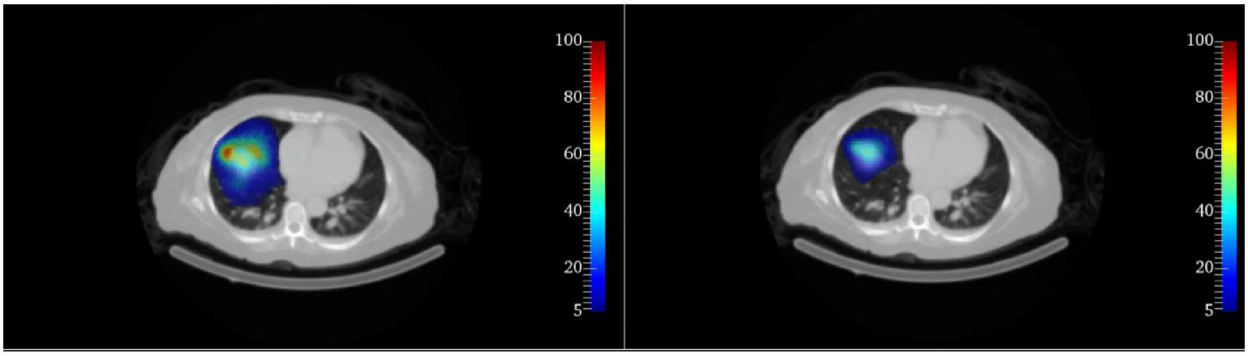

Figure 5.

Example of the differences for the calculated dose to lung using TOPAS (left) and MIRD scheme (right) for the pre-treatment imaging-based dosimetry of Patient 1. Color maps indicate Gy/GBq for the TOPAS and MIRD schema calculations.

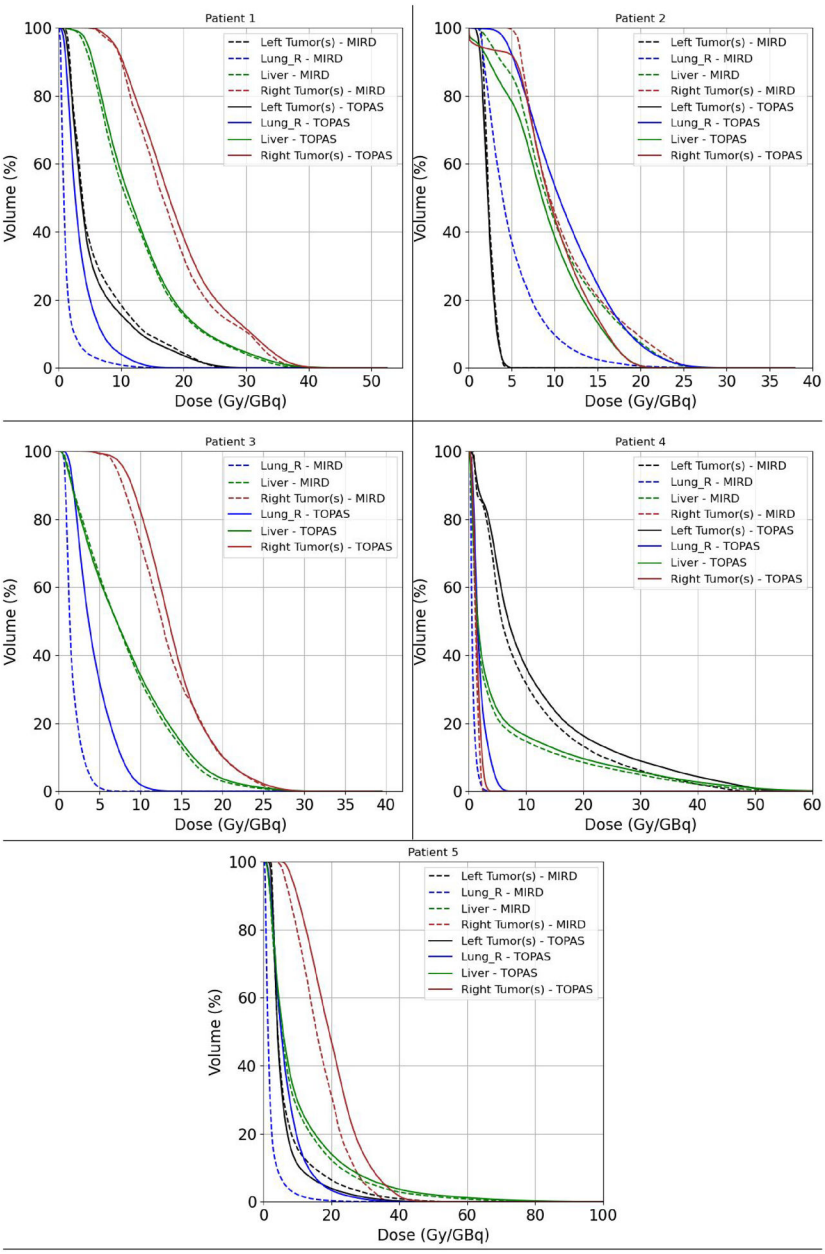

Figure 6.

Dose-volume histograms calculated with TOPAS and the MIRD schema for accumulated dose per GBq of activity in the ^{90}Y-SPECT image for each patient (post-treatment).

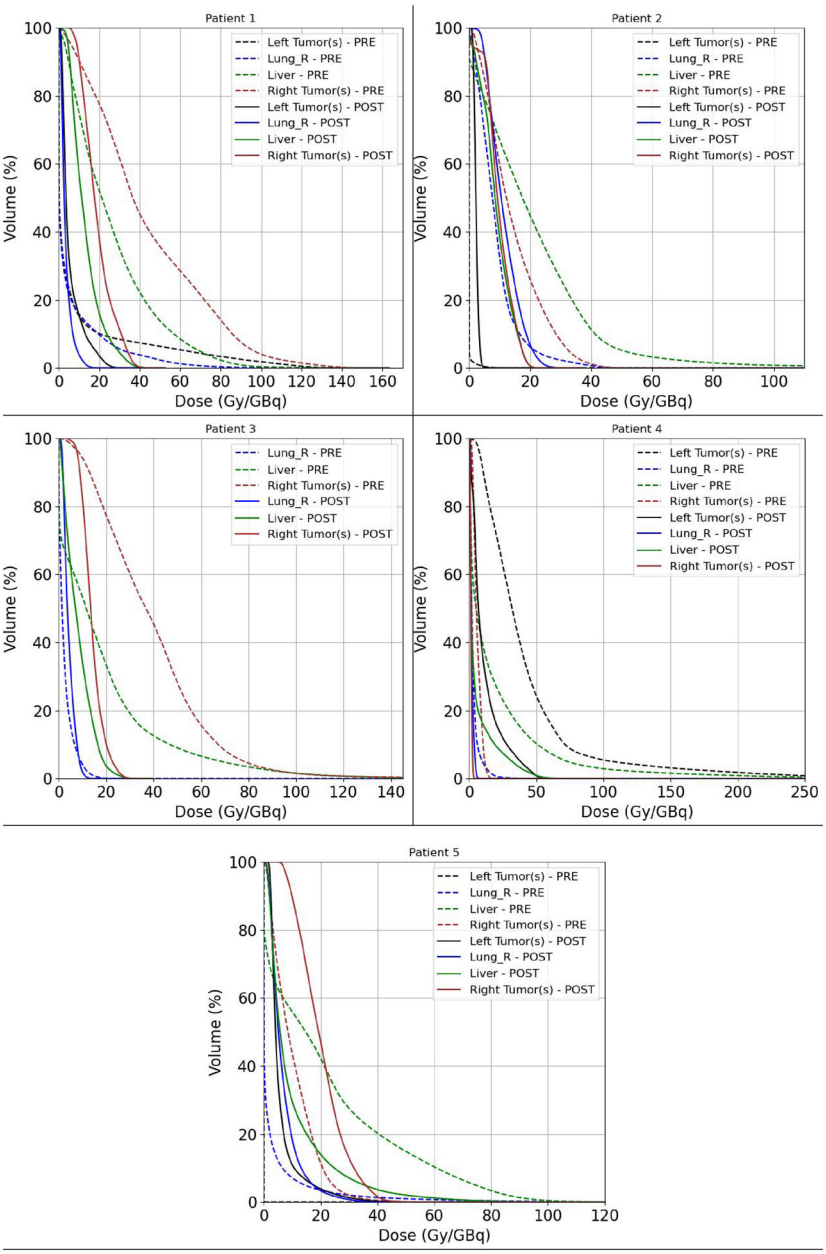

Figure 7.

Dose-volume histograms calculated with for accumulated dose per GBq of activity in both the ^{99m}Tc-MAA-SPECT and ^{90}Y-SPECT images for each patient (pre vs post-treatment)

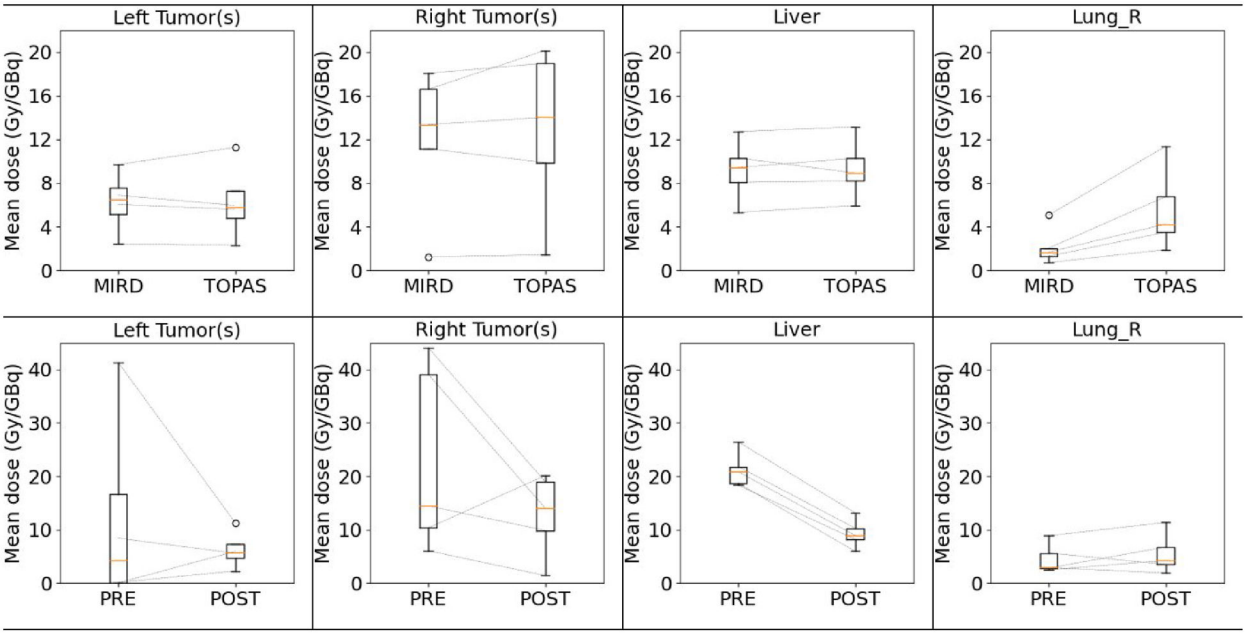

Figure 8.

Boxplots for mean doses per GBq calculated in the following structures: left and right tumors, liver and right lung. Top panels illustrate the difference between MIRD and TOPAS calculation using the ^{90}Y-SPECT images (post-treatment). Bottom panels show the differences in TOPAS-based dose calculation when employing pre and post-treatment imaging. Dotted lines represent individual differences for each patient.

Table 1.

Details of pre- and post-treatment imaging and treatment for each patient considered in this study. ^{90}Y delivery position difference is relative to the ^{99m}Tc-MAA catheter position.

	Patient 1	Patient 2	Patient 3	Patient 4	Patient 5
Total ^{90}Y activity (GBq)	1.07	2.69	4.07	3.47	4.48
Type of microsphere	Resin	Resin	Resin	Glass	Glass
^{99m}Tc-MAA delivery position	RHA	RHA	RHA	RHA	RHA
^{90}Y delivery position difference	RHA - 18 mm more distal	Split dose: CS VIII and CS VI/VII	Split dose: distal RAHB and RPHB	RHA - 15 mm more distal	Split dose: CS VII and CS IV
Days between CT/MR for contours & pre-treatment imaging	13 (MR)	21 (CT)	27 (CT)	19 (CT)	18 (CT)
Days between pre- & post-treatment imaging	9	21	8	14	8

RHA stands for right hepatic artery; LHA stands for left hepatic artery; CS stands for Couinaud Segment; RAHB stands for right anterior hepatic branch; RPHB stands for right posterior hepatic branch.